

1 **Fluorescence-based mapping of condensate dielectric permittivity uncovers**  
2 **hydrophobicity-driven membrane interactions**

3  
4 E. Sabri<sup>1</sup>, A. Mangiarotti<sup>1,2,3</sup> and R. Dimova<sup>1</sup>

5 <sup>1</sup>*Max Planck Institute of Colloids and Interfaces, Science Park Golm, 14476 Potsdam, Germany*

6 <sup>2</sup>*Centro de Investigaciones en Química Biológica de Córdoba (CIQUIBIC), CONICET,*  
7 *X5000HUA Córdoba, Argentina.*

8 <sup>3</sup>*Departamento de Química Biológica Ranwel Caputto, Facultad de Ciencias Químicas,*  
9 *Universidad Nacional de Córdoba, X5000HUA Córdoba, Argentina.*

10  
11  
12  
13 **ABSTRACT**

14  
15 Biomolecular condensates, essential for cellular organization, possess mesoscale properties  
16 largely governed by hydrophobicity, influencing molecule partitioning and material  
17 characteristics like viscosity, surface tension, and hydration. While hydrophobicity's role is  
18 increasingly recognized, its impact on membrane-condensate interactions remains unexplored.  
19 Here, we introduce a novel approach, combining hyperspectral imaging of an environment-  
20 sensitive dye and phasor analysis, to quantitatively map the local dielectric permittivity of both  
21 condensates and their environment with pixel resolution as sensed by the dye. This robust  
22 method reveals a surprisingly broad range of condensate permittivities, from oil-like to water-  
23 like. Importantly, we uncover that membrane affinity is not dictated by condensate permittivity  
24 itself, but by the permittivity contrast with their surroundings. Indeed, membrane wetting  
25 affinity is found to scale linearly with this contrast, unveiling a unifying dielectric principle  
26 governing condensate-membrane interactions. Compatible with live-cell and *in vitro* imaging,  
27 this technique provides unprecedented insights into condensate biophysics and function and  
28 opens new avenues for studying biomolecular condensate biology.

## 34 INTRODUCTION

35 Biomolecular condensates form as a result of liquid-liquid phase separation (LLPS) and are  
36 key to intracellular organization. Examples of these phase-separated compartments include  
37 membraneless organelles such as stress granules<sup>1</sup>, nucleoli<sup>2</sup>, mitochondrial nucleoids<sup>3</sup> and  
38 nuclear speckles<sup>4</sup>, which provide a dynamic and reversible means for cells to maintain  
39 homeostasis<sup>1,3,4</sup>, adapt to stress<sup>5-7</sup> and regulate biochemical processes spatially and temporally<sup>4,</sup>  
40 <sup>8,9</sup>. The unique biophysical properties of condensates, such as viscosity<sup>10-12</sup>, protein packing<sup>13,</sup>  
41 <sup>14</sup>, hydration<sup>7, 13, 14</sup>, pH<sup>15</sup>, surface tension<sup>11</sup> and electrostatic properties<sup>16</sup>, set them apart from  
42 their surrounding environment and are crucial for their diverse functions. In particular, the  
43 hydrophobicity and perceived micropolarity of condensates, have recently emerged as readily  
44 measurable characteristics exhibiting strong correlations with each of these physicochemical  
45 parameters<sup>9, 11, 17, 18</sup>.

46 While terms like “polarity”<sup>19, 20</sup> or “micropolarity”<sup>11, 18, 21</sup> are commonly encountered, their  
47 use can be misleading when referring to a material’s dielectric constant, or dielectric  
48 permittivity. Dielectric permittivity, a macroscopic-scale property, reflects not only the polarity  
49 of molecules (i.e. the degree of charge separation at the molecular scale) but critically, also their  
50 capacity to reorient in the presence of a transient electric field (e.g. originating from the  
51 transiently excited state of a dye dipole). A molecule can possess high intrinsic polarity (i.e., a  
52 pronounced charge separation) but if its rotational mobility is restricted, its contribution to the  
53 overall dielectric permittivity of the medium will be low, despite its high molecular polarity.  
54 Provided that the dipolar relaxation of water molecules is the main factor of molecular  
55 reorientation in biological samples<sup>22</sup>, we will primarily use the more suitable terms  
56 “hydrophobicity” or “dielectric permittivity”. To ensure broad accessibility and to align with  
57 existing terminology in certain contexts, we will also employ “micropolarity” where  
58 appropriate, particularly when referencing established measurement paradigms.

59 Among the various techniques used to characterize condensates, fluorescence-based imaging  
60 has emerged as a powerful tool due to its sensitivity, non-invasiveness and high spatial and  
61 temporal resolution<sup>11, 23-27</sup>. From a fundamental perspective, fluorescence-based approaches  
62 quantify micropolarity on a dielectric permittivity scale, relying on the degree to which water  
63 molecules can redshift or quench the emission of environment sensitive dyes<sup>11, 18-21</sup>. Notably,  
64 these permittivity-sensitive dyes can detect how changes in protein sequence and interactions  
65 influence condensate properties *in vitro* and *in vivo*<sup>11, 14, 28</sup>. Given these insights, it is reasonable  
66 to predict that the dielectric permittivity of condensates is a key determinant in modulating their  
67 interactions with surrounding cellular components, such as membrane-bound organelles and  
68 the cytoskeleton. However, this critical aspect remains largely unexplored, primarily due to  
69 technical challenges associated with quantifying micropolarity, and establishing reliable  
70 calibration curves<sup>11, 26</sup>. Furthermore, while many environment-sensitive fluorescent probes  
71 exist<sup>11, 18, 19, 21, 26, 29</sup>, their detection range is limited, failing to assess the sharp contrasts in  
72 dielectric properties which are hallmark features, endogenous to biological and bio-mimetic  
73 systems.

74 In this study, we introduce a robust, fluorescence-based method for quantifying the  
75 dielectric permittivity of biomolecular condensates and their surrounding environment. Our  
76 approach utilizes 2-acetyl-6-(dimethylamino)naphthalene (ACDAN), a dipolar relaxation-

77 sensitive dye<sup>30, 31</sup>, widely used to probe intracellular water activity<sup>32-34</sup>, macromolecular  
78 crowding<sup>22</sup> and membranous compartments<sup>31, 35</sup>. As with any solvatochromic probe, ACDAN  
79 reports the dielectric properties of its immediate molecular environment. While this dye has  
80 previously been employed to infer dipolar relaxation in biomolecular condensates, these  
81 applications relied on inherently qualitative, arbitrary unitless scales. Here, we overcome this  
82 limitation by proposing a rigorous framework to establish a quantitative and broadband  
83 estimation of condensate dielectric permittivity based on the spectral response of ACDAN.  
84 Importantly, our method enables a simultaneous measurement of the properties of both dense  
85 (condensate) and depleted (environment) phases.

86 Building on this, we investigated the hypothesis that condensates dielectric properties  
87 governs their interaction with cellular structures, particularly membranes. While prior work has  
88 shown that condensate-membrane affinity can depend on bilayer and protein hydrophobicity,  
89 even with unchanged membrane surface composition<sup>36, 37</sup>, the direct role of condensate  
90 dielectric properties in these interactions remained unclear. Our results demonstrate a clear  
91 correlation between membrane binding and the permittivity contrast between condensed and  
92 depleted phases, revealing that dielectric mismatch directly governs condensate-membrane  
93 affinity. These findings establish the permittivities of the coexisting phases as key quantifiable  
94 parameters for understanding how biomolecular condensates interact with diverse cellular  
95 structures such as membrane-bound organelles and – via modulation of surface adhesion  
96 energies – potentially other components such as the cytoskeleton.

97

## 98 **RESULTS**

### 99 **ACDAN hyperspectral imaging provides a highly sensitive readout of solvent permittivity**

100 The fluorescence of the ACDAN dye (Fig. 1a) is highly sensitive to solvent dipolar  
101 relaxation<sup>22, 31-35</sup>. Upon UV absorption, the dipole moment of ACDAN increases, generating a  
102 local electric field. Surrounding solvent molecules reorient to align with this field, lowering the  
103 energy of the dye-solvent system. This solvent reorganization leads to a redshift of the  
104 fluorescence emission, with larger shifts corresponding to environments of higher dielectric  
105 permittivity (Fig. 1b).

106 To translate this solvent-dependent spectral redshift into a quantitative measure of dielectric  
107 permittivity (i.e. build a calibration curve), we characterized ACDAN's spectral response in a  
108 broad panel of homogeneous solvents with known permittivity, using both hyperspectral  
109 microscopy (Fig. 1c,d) and spectrofluorimetry (see SI). While both approaches yield equivalent  
110 permittivity calibrations for homogeneous samples (Figs. S1–S3), spectrofluorimetry is limited  
111 to bulk (cuvette) measurements and lacks spatial resolution, limiting its ability to resolve  
112 distinct dielectric properties in phase-separated (or heterogeneous) samples. We therefore  
113 employ hyperspectral microscopy, which records a full emission spectrum at each image pixel,  
114 generating spatially resolved spectral maps (Fig. 1c,d). This allows local permittivity variations  
115 to be visualized directly within heterogeneous systems, including phase-separated biomolecular  
116 condensates.

117 To construct a calibration curve, we measured homogeneous reference solutions of known  
118 permittivity (Fig. 1d) and analyzed the spectra using two approaches: Gaussian fitting and a fit-  
119 free Fourier-space analysis based on spectral phasors<sup>22</sup>. Both methods yield equivalent results

120 for simple spectra, with the phasor approach offering additional robustness and extensibility for  
121 complex spectral profiles.

122 For the Gaussian fitting approach, spectral data from each solution were averaged across all  
123 pixels to obtain a robust emission curve (Fig. 1d), which was then fitted with a Gaussian  
124 function (Fig. 1c sketch and Methods). Figure 1e (orange data) presents the resulting calibration  
125 curve, linking ACDAN's maximum emission wavelength to solvent permittivity.

126 The phasor plot analysis involves computing the discretized Fourier transform of the dye  
127 emission spectrum and representing it as a single point in a two-dimensional "phasor plot" (Fig.  
128 1c, bottom right). The plot's modulus (distance from the center) provides information on the  
129 broadness of the spectrum, which can be affected by, e.g., fluorescence quenching<sup>38</sup>, while its  
130 phase (angular position) reflects the emission spectrum center of mass, which directly depends  
131 on the permittivity of fluorophore microenvironment<sup>22</sup> (Fig. 1c bottom right). In summary, the  
132 phasor plot analysis provides a fit-free representation of fluorescence spectra, allowing each  
133 pixel to be mapped onto a two-dimensional space where spectral shifts, rather than absolute  
134 intensity, can be directly visualized and compared. In this context, the phasor position serves  
135 as a compact descriptor of the local dielectric environment sensed by ACDAN.

136 For a hyperspectral image stack (Fig. 1c top left), the set of spectra measured at individual  
137 pixels yields a scatter plot (cloud) in the phasor space (as sketched in Fig. 1c bottom right). To  
138 map permittivity in a given system, we built a calibration curve by analyzing images of  
139 homogeneous solutions with known permittivity. This generated a reference phasor plot (Fig.  
140 S2), from which the phase was used to build the calibration curve Fig. 1f (orange data).

141 As a proof of principle, Fig. 1e,f includes a dataset for ethanol–water mixtures (blue data  
142 points), with dielectric constants estimated using the celebrated Maxwell-Garnett law of  
143 mixtures<sup>39</sup> (see Table S3 and Fig. S1c for spectra). These data serve as an additional validation  
144 that in these systems the ACDAN redshift reflects solvent permittivity rather than specific  
145 chemical interactions. We demonstrate in the SI that this approach yields equivalent results via  
146 spectrofluorimetry (Figs. S1-S3), and that a fit-free phasor representation in Fourier space also  
147 yields equivalent results to the Gaussian fit (see Figs. S1-S3).

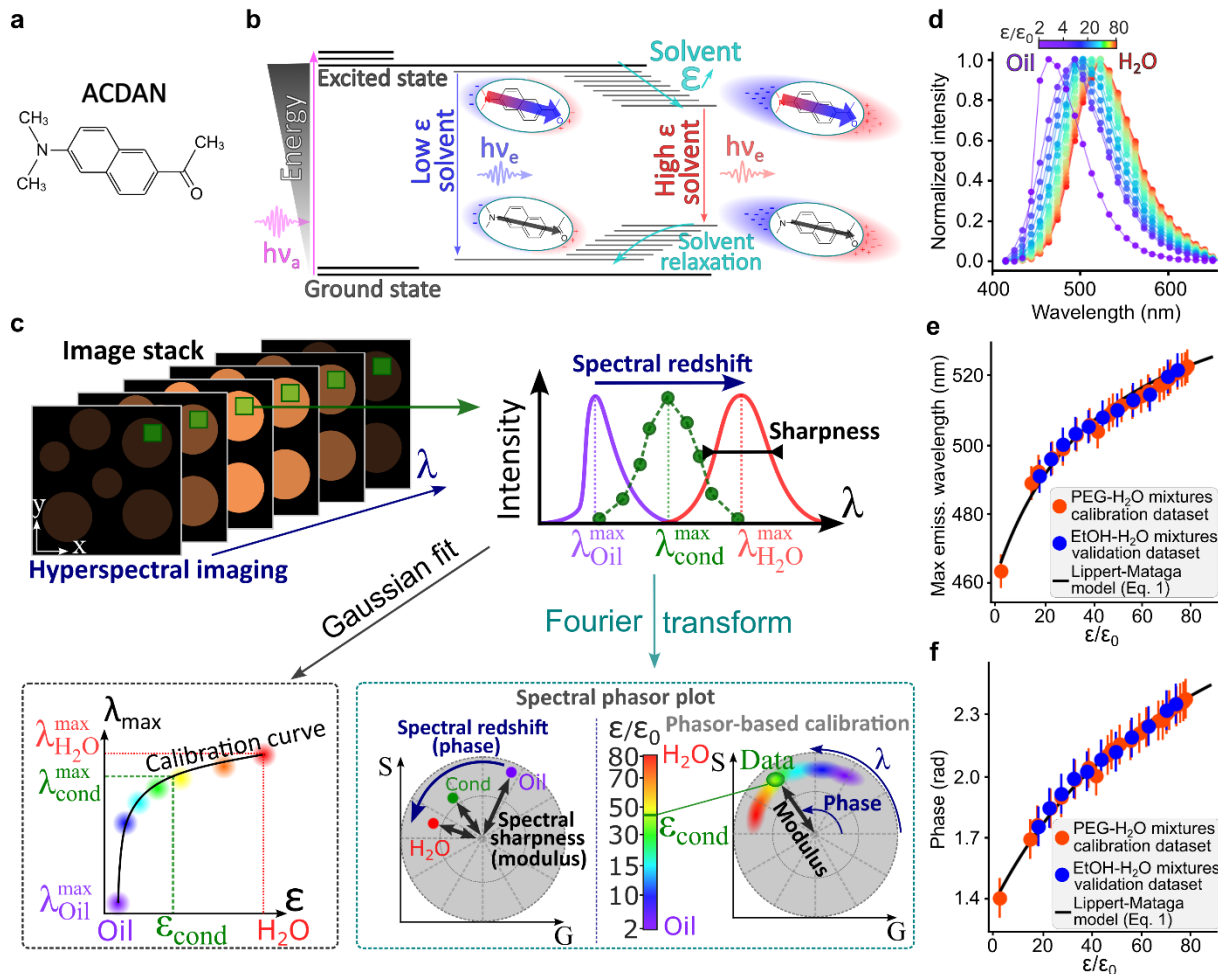
148 While both approaches yield equivalent results, this comparison serves several purposes: it  
149 verifies that our permittivity measurements are robust across analytical frameworks and  
150 instrumental platforms; it demonstrates that the canonical Gaussian fit, which encodes only the  
151 peak emission wavelength, can be matched by a fit-free, two-dimensional spectral phasor  
152 approach capturing both spectral redshift (phase) and broadening (modulus, reflecting  
153 quenching and spectral quality); and it shows that the phasor method can be applied to more  
154 complex spectra where simple Gaussian fitting is insufficient, enabling straightforward  
155 permittivity mapping in challenging systems<sup>14</sup>.

156 Additionally, Fig. 1e,f demonstrates that the redshift of ACDAN's emission spectrum is  
157 governed by a single physical quantity, namely the solvent dielectric permittivity. Importantly,  
158 this empirical observation is fully consistent with first-principles fluorescence theory, where  
159 according to the Lippert–Mataga relation<sup>38</sup>, dipole–dipole interactions between the fluorophore  
160 and its dielectric environment give rise to a predictable shift in the emission maximum (see SI).  
161 Indeed, the Lippert–Mataga equation accurately reproduces the calibration data obtained across  
162 a broad range of solvents (Fig. 1e,f solid curve), establishing a robust relationship between the  
163 maximum emission wavelength  $\lambda_{\text{max}}$  and solvent permittivity  $\epsilon$ :

164

$$\frac{1}{\lambda_{\max}} \sim \mu_E \frac{(\mu_G - \mu_E)}{V_{dye} h c} f(\epsilon) + \text{const}, \quad (1)$$

165 where  $\mu_E$  and  $\mu_G$  are the excited state and ground state dipole moments of the fluorophore,  $V_{dye}$   
 166 is the effective molecular volume of ACDAN,  $h$  is the Planck constant,  $c$  is the speed of light  
 167 in vacuum, and  $f(\epsilon)$  is the generalized Debye function (see SI for full model description).  
 168 While Eq. 1 accurately describes the hyperspectral imaging data (Fig. 1e,f), it shows  
 169 discrepancies with the spectrofluorimetry data, for which an empirical logarithmic function  
 170 provided a better fit (see Fig. S1d and SI text for discussion).  
 171



172

173

174 **Figure 1: ACDAN hyperspectral imaging enables spatial mapping of dielectric permittivity with**

175 **pixel resolution.** (a) Molecular structure of the ACDAN (6-acetyl-2-dimethylaminonaphthalene)

176 fluorescent probe, a water-soluble molecule that partitions in biomolecular condensates. (b) Perrin-

177 Jablonsky diagram illustrating the dependence of ACDAN fluorescence on solvent permittivity. The

178 sketch depicts changes in ACDAN dipole moment due to photon absorption or emission and the solvent

179 relaxation process. In low permittivity solvents, weak dipolar relaxation results in minimal redshift of

180 the dye's fluorescence. Conversely, highly polar solvents lead to strong redshift due to enhanced solvent

181 relaxation and a greater decrease in the energy gap for emission.  $h\nu_a$  and  $h\nu_e$  represent the absorption

182 and emission energies, respectively. (c) Schematic representation of confocal hyperspectral imaging and

183 analysis. A full emission spectrum is measured at each pixel from a stack of images acquired at different

184 wavelengths ( $\lambda$ ). The pixel permittivity (for either condensed or depleted phases) can be determined

185 using two approaches: Gaussian fitting (bottom left) and phasor representation (bottom right). In the

186 Gaussian fitting approach, the wavelength of maximum emission  $\lambda_{\max}$  is plotted as a function of reported

187 permittivity values to obtain a calibration curve; see panel (e) and text for details. In the phasor

188 representation, the spectral information from each pixel in an image is first processed via a discrete

188 Fourier transform, and the resulting real (G) and imaginary (S) components define a point in a two-  
189 dimensional phasor space. The phase (reflecting the degree of emission redshift) and modulus (reflecting  
190 spectrum sharpness) of these points can be calibrated against reference permittivity values (graduated  
191 in the color bar) to map permittivity (see panel f and text for details). **(d)** Fluorescence emission profiles  
192 of ACDAN from hyperspectral microscopy imaging of calibration solutions of mineral oil or PEG400-  
193 H<sub>2</sub>O solutions (from left to right: 100%, 90%, 80%, 70%, 60%, 50%, 45%, 40%, 35%, 30%, 25%, 20%,  
194 15%, 10%, 8%, 6%, 4%, 2%, 1%, 0.5%, 0% PEG content). **(e, f)** Calibration data using the maximum  
195 emission wavelength of ACDAN obtained from a Gaussian fit of the spectrum (e) or the phase in the  
196 phasor plot (f) as a function of previously reported or theoretically calculated solvent dielectric constant  
197 ( $\epsilon$ ): Orange circles represent different PEG-400 solutions in water, with permittivity values from  
198 literature (referenced in Table S1). Blue circles represent ethanol-water mixtures, with dielectric  
199 constants calculated using the Maxwell-Garnett law of mixtures (see SI, Table S3 and Fig. S4b). The  
200 relation  $\frac{\phi(\lambda_f - \lambda_0)}{2\pi} + \lambda_0 = \lambda_{\max}$  with  $\lambda_0 = 416\text{nm}$  and  $\lambda_f = 728\text{nm}$  was used to establish the link  
201 between the emission wavelength  $\lambda_{\max}$ , and the phase  $\phi$  for which the Lippert-Mataga equation (Eq. 1,  
202 solid curve; fitting parameters given in Table S2) accurately describes the data.

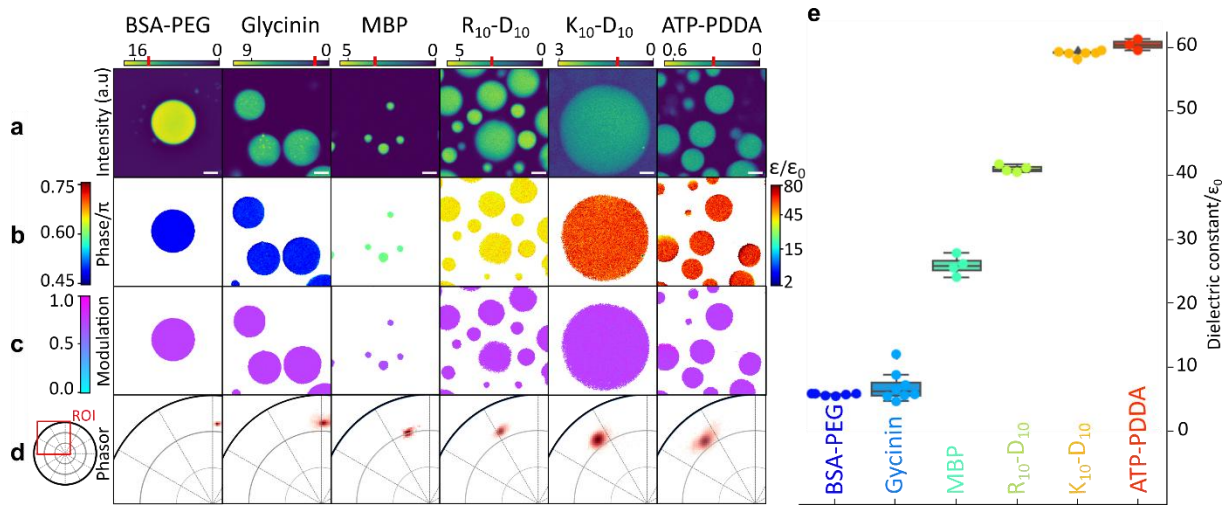
203  
204 Taken together, our results demonstrate that ACDAN emission provides a sensitive and  
205 broadband readout of dielectric permittivity ( $2 - 80\epsilon_0$ ). The close agreement between our  
206 calibration and validation datasets (Fig. 1e,f) demonstrates robust sensitivity that is consistent  
207 across different solvent chemistries and independent of the measurement platform (microscopy  
208 or spectrofluorimetry). In these systems, ACDAN behaves as a passive solvatochromic probe,  
209 allowing us to treat the dye emission redshift, quantified by  $\lambda_{\max}$ , as a bijective function of the  
210 permittivity of the dye immediate microenvironment: each  $\lambda_{\max}$  corresponds to a unique  
211 permittivity  $\epsilon$ , and vice versa. While we expect this relationship to hold broadly, potential  
212 limitations in systems containing folded proteins with specific binding sites are addressed in  
213 the discussion section.

214 In the following, we employ the microscopy-based hyperspectral imaging approach for data  
215 acquisition and the spectral phasor-based framework (Fig. 1c) to resolve biomolecular  
216 condensates permittivity (calibration detailed in Fig. S2). We chose this framework for two key  
217 reasons: first, its lack of requirement for an analytical fit function, especially relevant for probes  
218 with complex emission spectra (e.g. LAURDAN<sup>14</sup> or multifunctional fluorescent probes<sup>21, 40</sup>)  
219 that are not accurately described by Gaussian models; second, it exhibits superior accuracy,  
220 with a maximum error of 8% compared to 13% for Gaussian fitting (Table S3).

## 221 222 **Hyperspectral imaging allows determination of biomolecular condensates permittivity**

223 To evaluate condensate permittivity, we analyzed six different systems, for which three  
224 distinctive types of LLPS can be identified: (i) segregative LLPS in polyethylene-glycol (PEG)-  
225 bovine serum albumin (BSA), and PEG-dextran solutions, (ii) self-coacervation in myelin basic  
226 protein (MBP) and soy-plant based glycinin condensates, and (iii) complex coacervation in  
227 adenosine triphosphate (ATP)-polydiallyldimethylammonium chloride (PDDA), and  
228 oligopeptides-based condensates made of poly-lysine (K)-poly-aspartic acid (D) (K<sub>10</sub>-D<sub>10</sub>) and  
229 poly-arginine (R)-poly-aspartic acid (D) (R<sub>10</sub>-D<sub>10</sub>). Among these, the PEG-dextran, glycinin,  
230 and PEG-BSA systems were chosen for their cost-effectiveness and the feasibility of physically  
231 separating and analyzing their individual coexisting phases, facilitating more systematic  
232 characterization. The results of the phasor-based analysis of hyperspectral stacks for these  
233 systems are presented in Fig. 2. In this figure, the 2D phasor representation allows us to

234 precisely distinguish between two metrics of interest encoded in the spatial coordinates; the  
 235 *phase* reports on ACDAN redshift and encodes condensate permittivity (panel b) and the  
 236 *modulus* reports on spectral sharpness and encodes dye emission quenching (panel c).  
 237



238 **Figure 2: ACDAN hyperspectral imaging enables the broad-range determination of local**  
 239 **permittivity in biomolecular condensate dense phase.** (a) Representative mean intensity images  
 240 (averaged over the entire detected spectral range) of various biomolecular condensate systems, as  
 241 labeled. Upper color bars indicate fluorescence intensity (arbitrary units), with red marks denoting the  
 242 pixel exclusion threshold applied to panels b-d. Scale bars: 5μm. (b) Local dielectric permittivity maps  
 243 (right color bar) derived from the spectral phase (left color bar). The spectral phase, which roughly  
 244 reflects the emission maximum (see Fig. 1d and Methods), is translated into permittivity values using  
 245 the microscopy-based phasor calibration curve (Fig. 1f). (c) Maps of spectral modulus (left color bar),  
 246 reflecting spectrum broadness (Fig. 1c, Methods) showing only minor differences across condensate  
 247 systems. (d) Phasor plot representation of the spectral information. Each dot represents the phase and  
 248 modulus of an individual pixel from the image stacks in (a). The left inset highlights the region of interest  
 249 (ROI) covering the experimental permittivity range (from 2ε<sub>0</sub> to 80ε<sub>0</sub>). The spread of the pixel cloud  
 250 illustrates the measurement error. (e) Dielectric permittivity values for all imaged condensate systems  
 251 span a surprisingly broad range from ~5ε<sub>0</sub> (comparable to oil-like environments) to ~60ε<sub>0</sub> (closer to  
 252 water) as sensed in the immediate environment of ACDAN. Each dot represents data from a stack of  
 253 images. Box plots indicate mean±SD (BSA-PEG and K<sub>10</sub>-D<sub>10</sub>: n=6, glycinin: n=8, ATP-PDDA: n=3,  
 254 R<sub>10</sub>-D<sub>10</sub> and MBP: n=4); see Fig. S4 for additional statistical details and experimental conditions.  
 255  
 256

257 Panels (b-d) of Fig. 2 were produced by applying a minimal intensity threshold to identify  
 258 the highest intensity portion of the data in panel (a). This procedure distinguished condensates  
 259 already settled at the bottom of the imaging chamber (highest mean signal) from those  
 260 sedimenting into the observation plane during acquisition (moderate to low mean signal). The  
 261 latter exhibited artificially elevated permittivity due to the absence of shorter-wavelength  
 262 spectral components and were therefore excluded from the analysis as indicated in Fig. 2a.

263 We also observed that BSA-PEG condensates display higher fluorescence intensity, likely  
 264 reflecting an increased quantum yield of ACDAN and a known tendency of the “sticky” BSA  
 265 protein to bind small molecules<sup>41</sup>. As a solvatochromic fluorophore, ACDAN probes the  
 266 dielectric properties in its immediate molecular vicinity rather than a bulk-averaged  
 267 environment; in this case, the enhanced signal suggests that the measured permittivity  
 268 predominantly reflects protein-proximal microenvironments rather than a simple bulk average  
 269 (see Discussion).

270 Figure 2b-c shows that while phase values (encoding dye redshift, Fig. S2), and thus  
271 permittivity (Fig. 2b), vary significantly among condensate systems, the modulus (related to  
272 spectra sharpness, Fig. S2) only slightly decreases with increasing permittivity (Fig. 2c). This  
273 observation is further evident in Fig. 2d and consistent with the expected fluorescence  
274 quenching effect associated with dipolar relaxation<sup>38</sup>. The spread of the pixel cloud in Fig. 2d  
275 visually illustrates measurement error, which is inversely proportional to the signal-to-noise  
276 ratio.

277 Averaging the phase values and converting them to permittivity yields Fig. 2e (additional  
278 statistical details in Fig. S4). The data reveal a remarkably broad range of dielectric constants  
279 across different condensates, from values as low as  $\sim 5\epsilon_0$  (typical of oil-like environments) to as  
280 high as  $\sim 60\epsilon_0$  (approaching that of water), highlighting substantial variability in condensate  
281 hydrophobicity as sensed by ACDAN. Additionally, the weak correlation between the type of  
282 interaction driving LLPS and condensate permittivity (Fig. 2e) suggests that condensate  
283 dielectric properties cannot be predicted solely based on the type of LLPS mechanism. A  
284 striking example is the comparison between K<sub>10</sub>-D<sub>10</sub> and R<sub>10</sub>-D<sub>10</sub> condensates both formed via  
285 similar electrostatic heterotypic interactions; despite only four-atom difference between lysin  
286 and arginine, their permittivities differ drastically, i.e. by  $\sim 20\epsilon_0$  (Fig. 2e). These observations  
287 are consistent with *in silico* assessments of differential hydration energies in arginine- versus  
288 lysin-rich assemblies<sup>42, 43</sup>.

289

### 290 **Dielectric permittivity as a descriptor of condensed and dilute phases**

291 Changes in macromolecules concentration within either the dense or depleted phase  
292 modulate protein hydration and water activity, thereby altering the permittivity contrast  
293 between the two phases<sup>2, 11, 44</sup>. Thermodynamically, such shifts reflect changes in the system  
294 position on its phase diagram<sup>45</sup>. From this perspective, measuring the permittivity contrast  
295 between two coexisting phases provides a qualitative readout of a mixture's phase state.  
296 Hyperspectral imaging of ACDAN as applied here, enables simultaneous determination of the  
297 permittivity of coexisting phases, from which changes in the position of a mixture within its  
298 phase diagram can be inferred, as illustrated in Fig 3.

299 As a benchmark system, we first examine a canonical aqueous two-phase system (ATPS)  
300 composed of PEG and dextran. At low polymer concentrations, they form a homogeneous  
301 aqueous solution, while increasing the concentration of either polymer induces LLPS into a  
302 PEG-rich phase and a dextran-rich dense phase (Fig. 3a). This PEG-dextran ATPS is a well-  
303 established model system with robustly characterized phase diagrams (see e.g. ref. <sup>46</sup>), making  
304 it ideally suited to validate our approach and to systematically track how dielectric permittivity  
305 varies with macromolecular composition.

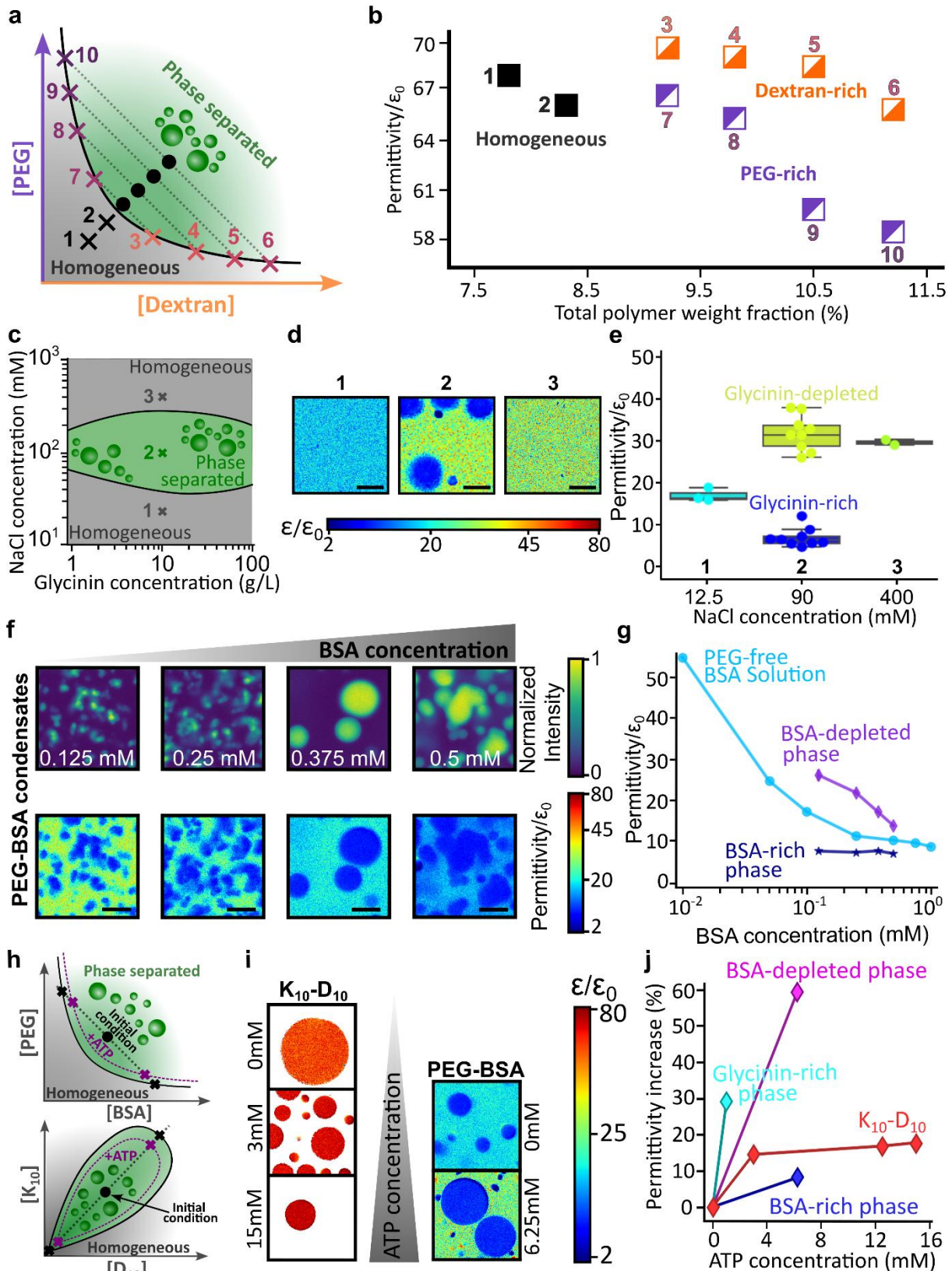
306 Although water is present in both phases (making this formally a ternary system) the PEG-  
307 dextran phase diagram and tie lines provide a way to evaluate the water content and  
308 macromolecular crowding in each phase based on changes in polymer concentration. Building  
309 on this knowledge, Figure 3b illustrates how variations in the initial PEG and dextran  
310 concentrations, schematically indicated as points in the phase diagram (Fig. 3a), translate into  
311 distinct permittivity values.

312 Measurements for points (3–10) in Fig. 3a,b were performed by isolating the PEG-rich and  
313 dextran-rich phases of the ATPS; corresponding permittivity maps and phase compositions are

314 provided in Fig. S5 and Table S4. Even a small increase in polymer concentration (a few tens  
315 of percent), accompanied by a reduction in water fraction, consistently results in lower  
316 permittivity, corroborating previous reports<sup>47</sup>. Moreover, Fig. 3a,b shows that changes in total  
317 polymer concentration (crosses 1 and 2 for homogeneous and black dots for phase separated  
318 solutions in panel a) result in different levels of macromolecular crowding and water content in  
319 both homogeneous and phase-separated regimes, which are quantitatively reflected in the  
320 measured permittivity values.

321 Figure 3c-g further emphasizes the generality of these trends, displaying data for glycinin  
322 and PEG-BSA systems. Figure 3c-e shows that different points in the glycinin phase diagram  
323 (Fig. 3c) correspond to markedly different permittivity values between homogeneous and phase  
324 separated states. Similarly, Fig. 3f shows that increasing the overall BSA concentration  
325 decreases the permittivity of the BSA-depleted phase, a trend quantified in Fig. 3g and  
326 compared to PEG-free BSA aqueous solutions.

327  
328  
329  
330



331  
 332 **Figure 3: Hyperspectral mapping of dielectric permittivity across condensed and dilute phases.**  
 333 (a) Sketch of a PEG-dextran phase diagram, see <sup>45</sup> for experimental values. Crosses (1-2) represent  
 334 homogeneous PEG-dextran solutions. Black dots indicate the initial polymer concentration of the tested  
 335 phase-separated mixtures. The binodal is shown by a black curve and grey dotted lines represent the tie  
 336 lines. The endpoints of the tie lines indicate the dextran-rich phase compositions (crosses 3-6) and the  
 337 PEG-rich phase compositions (7-10). (b) Permittivities of homogeneous and phase separated solutions

338 at different total polymer concentration. The labels next to the data points correspond to the  
339 compositions schematically presented in panel (a), see Fig. S5 for hyperspectral maps and Table S4 for  
340 exact compositions. (c) Phase diagram of glycinin condensation as a function of protein and NaCl  
341 concentrations, experimentally determined in <sup>48</sup>. Grey regions indicate homogeneous mixtures and the  
342 green region denotes phase separation (condensate formation). Points 1, 2 and 3 correspond to NaCl  
343 concentrations of 12.5, 100, and 400 mM, respectively, at a constant protein concentration of 10 g/L.  
344 (d) Example permittivity maps for glycinin solutions at three NaCl concentrations indicated in (c). The  
345 color bar represents rescaled permittivity. Scale bars: 10  $\mu\text{m}$ . (e) Quantified permittivity of all phases at  
346 points 1, 2 and 3 in (c, d). (f) Effect of BSA concentration on the permittivity of PEG-BSA condensate  
347 systems. Top: average intensity projections of hyperspectral stacks for different initial BSA  
348 concentrations (indicated in white). Bottom: corresponding permittivity maps of the same regions,  
349 showing a gradual decrease in the depleted phase permittivity with increasing protein concentration.  
350 Scale bars: 10  $\mu\text{m}$ . (g) Increasing the total BSA concentration lowers the permittivity of homogeneous  
351 protein solutions in water (blue circles) and BSA-depleted phase (diamonds), but has no significant  
352 effect on the PEG-BSA condensates (stars); see Fig. S6 for the respective permittivity maps. (h)  
353 Schematic phase diagrams illustrating the expected phase behavior of the PEG-BSA system (top) and  
354 the K<sub>10</sub>-D<sub>10</sub> system (bottom). The solid black curves denote the binodals, and the black dotted lines  
355 represent tie lines through the initial overall composition (black dot). Black crosses indicate the  
356 compositions of the coexisting dense and depleted phases in the absence of ATP. The purple dotted  
357 curves illustrate the expected shift of the binodal upon ATP addition, reflecting weakened intermolecular  
358 interactions. Correspondingly, purple crosses indicate the altered compositions of the coexisting phases  
359 in the presence of ATP. (i) Permittivity maps illustrating the effect of increasing ATP concentration on  
360 K<sub>10</sub>-D<sub>10</sub> and BSA-PEG condensates. Each frame represents a 36.9 $\times$ 36.9  $\mu\text{m}^2$  sample area. The color bar  
361 (logarithmic scale) indicates permittivity. Left: permittivity maps of K<sub>10</sub>-D<sub>10</sub> condensates showing  
362 increasing permittivity with ATP concentration. Right: permittivity maps of BSA-PEG condensates  
363 (10wt% PEG, 0.375 mM BSA) demonstrating a similar trend. (j) Impact of ATP concentration on the  
364 permittivity of K<sub>10</sub>-D<sub>10</sub>, and BSA-PEG (condensates shown in i) and glycinin condensates (10 g/L total  
365 protein in 100 mM NaCl). Permittivity values in the absence of ATP are given in Fig. 2.

366  
367 Figure 3a-g establishes that changes in macromolecular crowding systematically translate  
368 into variations in permittivity sensed by ACDAN across a range of phase-separated systems,  
369 with magnitudes that depend strongly on the molecular nature of the macromolecules. In  
370 segregative phase separation, increasing PEG or dextran concentrations (Fig. 3a,b), as well as  
371 increasing BSA concentration (Fig. 3f,g), enhance macromolecular crowding, leading to higher  
372 polymer or protein concentrations in both coexisting phases. These changes are consistently  
373 reflected by a reduction in the measured permittivity in each phase.

374 Similarly, Fig. 3c-e shows that increasing NaCl concentration above the lower critical point  
375 of glycinin solutions induces protein condensation, leading to a pronounced increase in  
376 macromolecular crowding within the dense phase, which is accompanied by a marked decrease  
377 in permittivity. Importantly, Fig. S7 presents spectrofluorimetric controls demonstrating that  
378 NaCl concentration alone does not substantially affect ACDAN fluorescence. Consistent  
379 microscopy-based controls confirming the salt insensitivity of ACDAN emission have been  
380 reported previously<sup>14</sup>. Together, these results demonstrate that macromolecular crowding and  
381 ionic conditions influence ACDAN emission indirectly, through their impact on the local  
382 dielectric environment sensed by the probe.

383 Permittivity measurements in PEG-BSA phase-separated systems further illustrate how the  
384 dielectric microenvironment differs between condensed and depleted phases. In these mixtures,  
385 both protein and polymer concentrations vary simultaneously across coexisting phases, and  
386 PEG itself strongly influences the permittivity (Fig. 3a,b). Thus, permittivity values as sensed

387 by ACDAN reflect the combined effects of water content, macromolecular crowding, but,  
388 importantly, also local probe–microenvironment interactions as we discuss below.

389 To further assess the sensitivity of our method to subtle physicochemical changes, we  
390 investigated the effects of ATP as a hydrotrope – a small molecule known to enhance protein  
391 solubility and hydration<sup>49-51</sup> – and examined its effect on the dielectric permittivity of various  
392 condensate systems. Figure 3h schematically summarizes the expected effects of ATP addition  
393 on the phase behavior of the investigated systems. ATP acts to weaken the intermolecular  
394 interactions that drive phase separation, resulting in a lower macromolecule concentration (and  
395 correspondingly higher water content) within the dense phase, alongside an increased  
396 protein/polymer concentration in the depleted phase. In the phase diagram representation, this  
397 manifests as a shift of the binodal boundaries away from the origin upon ATP addition,  
398 consistent with the observed reduction in permittivity contrast between coexisting phases as  
399 shown in Fig. 3i,j.

400 These results underscore the sensitivity of this method in detecting subtle variations in  
401 hydration and microenvironment within both condensed and depleted phases. Specifically,  
402 adding just a small amount of ATP progressively increases the permittivity of glycinin and K<sub>10</sub>-  
403 D<sub>10</sub> condensates by approximately 25% and 15%, respectively (Fig. 3i). Similar trends are  
404 observed in the BSA-PEG system, where the depleted phase permittivity increases by 60%  
405 upon addition of 6.25 mM ATP, compared to a modest 8% increase for the condensed phase.  
406 These differential responses suggest that ATP shifts the system’s position on its phase diagram  
407 (Fig. 3h) by selectively altering the hydration and dielectric permittivity of the coexisting  
408 phases.

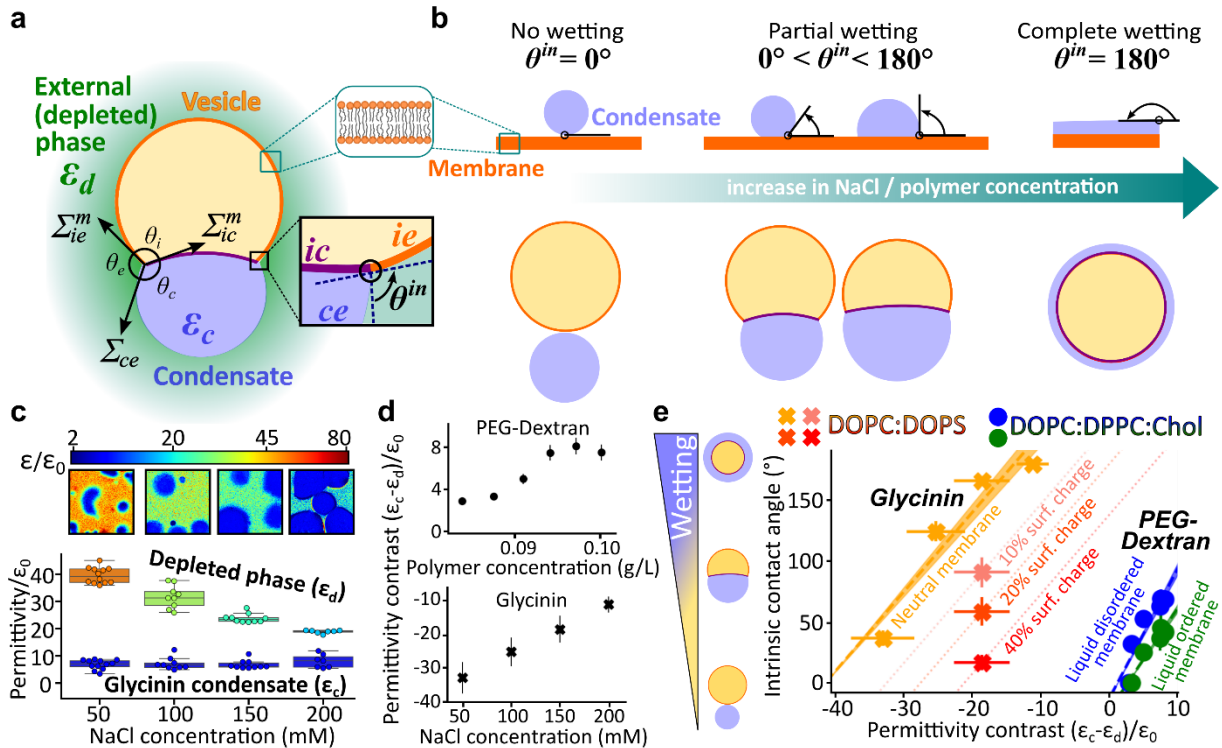
409 Overall, these findings demonstrate that permittivity measurements provide a sensitive  
410 readout of changes in dielectric microenvironment within coexisting phases, enabling  
411 qualitative tracking of how phase behavior responds to molecular perturbations such as ATP,  
412 without relying on assumptions about phase composition.

413

#### 414 **Permittivity contrast between dense and depleted phases governs condensate-membrane** 415 **interaction**

416 Building on the hypothesis that condensate hydrophobicity governs interactions with cellular  
417 structures like membranes, we investigated whether dielectric properties directly influence  
418 condensate-membrane affinity. Previous work shows that condensate-membrane interactions  
419 vary with bilayer hydrophobicity, modulated by, for example, lipid tails saturation, even when  
420 membrane surface chemistry (lipid headgroups) remains unchanged<sup>36</sup>. This intuitively suggests  
421 that condensate hydrophobicity, quantified through permittivity, may govern this interaction.

422 Upon contacting a membrane, condensates undergo a wetting transition reflecting the  
423 strength of their interaction<sup>52</sup>. This leads to mutual reshaping of both the membrane and the  
424 condensate<sup>53</sup>, where the resulting equilibrium morphology directly reflects the interaction  
425 affinity. Figure 4a,b presents examples of such a morphologies, observed during the interaction  
426 of condensates with membranes<sup>54</sup>, exemplified here by giant unilamellar vesicles, and well-  
427 described by the theoretical framework introduced in ref. <sup>53</sup>.



429

430

431

432

433

434

435

436

437

438

439

440

441

442

443

444

445

446

447

448

449

450

451

452

453

454

455

456

457

458

459

**Figure 4: Membrane wetting by condensates is modulated by the permittivity contrast between coexisting phases.** (a) Schematic illustration of a giant unilamellar vesicle (yellow) wetted by a condensate (blue, permittivity  $\epsilon_c$ ) and surrounded by the polymer-depleted phase (light green, permittivity  $\epsilon_d$ ). The apparent contact angles facing the vesicle interior ( $\theta_i$ ), the external phase ( $\theta_e$ ), and the condensate ( $\theta_c$ ), define the system equilibrium morphology. These angles, measured from confocal cross-sections of giant vesicles in contact with condensates, reflect a balance of interfacial forces at the three-phase contact line (black circle): the condensate interfacial tension  $\Sigma_{ce}$ , and the mechanical tensions of the two membrane segments in contact with the depleted condensate-free phase ( $\Sigma_{ie}^m$ , orange) and condensate phase ( $\Sigma_{ic}^m$ , purple). At the nanometer scale, the membrane does not exhibit a kink but is smoothly curved (inset), and wetting is described by the intrinsic contact angle  $\theta_{\square}^{in} = \arccos\left(\frac{\sin \theta_e - \sin \theta_c}{\sin \theta_i}\right)^{53}$ , see Methods. (b) Schematic illustrations of condensate wetting flat lipid membranes (top) and vesicles (bottom) illustrating distinct affinity regimes quantified by the intrinsic contact angle  $\theta_{\square}^{in}$  defined in (a) and characteristic morphologies. Increasing polymer or salt concentration enhances the membrane affinity of dextran and glycinin condensates<sup>45, 53</sup>. (c) Hyperspectral permittivity maps of glycinin condensates at increasing NaCl concentrations. Top: dielectric maps of fields of view ( $36.9 \times 36.9 \mu\text{m}^2$ ). The color bar represents the logarithmic permittivity scale. Bottom: boxplot showing that increasing salt primarily lowers the permittivity of the condensate-free (depleted) phase, while the condensate phase remains relatively unaffected. (d) Permittivity contrasts ( $\epsilon_c - \epsilon_d$ ) between dense (condensate) and external (depleted) phases as a function of polymer concentration (PEG-dextran, top, data from Figs. 3b and S5), and ionic strength (glycinin-NaCl, bottom, data from panel (c)). (e) The intrinsic contact angle  $\theta_{\square}^{in}$ , describing condensate-membrane affinity, increases linearly with the permittivity contrast ( $\epsilon_c - \epsilon_d$ ), indicating that stronger permittivity differences enhance membrane wetting by the condensate as illustrated schematically on the left. All experimental datasets were fitted with a linear function (dashed lines). Crosses display  $\theta_{\square}^{in}$  data from ref. <sup>53</sup> for glycinin condensates interacting with DOPC:DOPS membranes at various NaCl concentrations (pure DOPC, orange), and for 100 mM NaCl but different charged lipid content (10, 20 and 40 mol% DOPS, respectively shown in rose, vermilion and red); the respective permittivity contrast  $\epsilon_c - \epsilon_d$  is from panel (c). Dotted lines passing through data points for DOPS-doped membranes have the same slope as the charge-free membrane and serve as guides to the eye. Circles show  $\theta_{\square}^{in}$  data from ref. <sup>45</sup> for PEG-dextran ATPS droplets at different polymer concentrations in contact with either liquid-

460 disordered (DOPC:DPPC:Chol, 64:15:21, blue) or liquid-ordered (DOPC:DPPC:Chol, 13:44:43, green)  
461 membranes. The corresponding permittivity contrasts were interpolated from data presented in Fig. 3b.  
462

463 The force balance between the tensions of the wetted ( $\Sigma_{ic}^m$ ) and bare ( $\Sigma_{ie}^m$ ) membrane  
464 segments and the condensate interfacial tension ( $\Sigma_{ce}$ )<sup>53, 55</sup> (see Methods) shapes the vesicle-  
465 condensate couple into an axisymmetric system characterized by three apparent contact angles  
466 ( $\theta_i, \theta_c, \theta_e$ ) (Fig. 4a and Methods). These apparent contact angles are extracted from confocal  
467 cross-sections passing through the symmetry axis of the vesicle–condensate system. While they  
468 fully describe the observed geometry, their values depend on extrinsic parameters such as  
469 condensate and vesicle size, as well as the degree of vesicle deflation, which vary between  
470 individual vesicle–condensate pairs in a sample. By contrast, at the nanometer scale, the  
471 membrane is smoothly curved at the three-phase contact line (black circle in Fig. 4a)<sup>56</sup> and  
472 wetting is characterized by the intrinsic contact angle  $\theta_{\square}^{in}$ <sup>57</sup>. This intrinsic angle is a material  
473 parameter that is independent of system geometry or size<sup>53</sup> and quantifies the membrane  
474 preferential affinity for the protein-rich (condensed) versus protein-poor (depleted) phase<sup>53</sup>.  
475 While  $\theta_{\square}^{in}$  has been shown to vary with salt, polymer or protein concentration<sup>14, 45, 52</sup>, membrane  
476 charge<sup>14</sup> and lipid composition<sup>36</sup>, the fundamental basis underlying these variations remains  
477 unclear. Intuitively, one might expect that a condensate with a permittivity similar to that of the  
478 membrane would exhibit stronger affinity. However, the intrinsic contact angle reflects not the  
479 absolute affinity of one phase for the membrane, but rather the relative affinities of the two  
480 coexisting aqueous phases, see Methods. Because the sum of the contact angles opening toward  
481 each phase must equal  $180^\circ$  (see inset in Fig. 4a), a change in membrane preference for one  
482 phase necessarily implies a corresponding change for the other.

483 As a first step to test this hypothesis, we quantified the permittivities of coexisting phases in  
484 heterogeneous glycinin solutions and PEG-dextran APTS. While the permittivity of the  
485 glycinin-depleted phase exhibited decrease markedly with increasing salt concentration, the  
486 condensed phase remained unaffected (Fig. 4c). This led to a monotonic decrease in the  
487 permittivity contrast ( $\epsilon_c - \epsilon_d$ ), see Fig. 4d (top). For PEG-dextran mixtures, increasing polymer  
488 concentration caused both phases to become less polar, with a stronger permittivity drop in the  
489 PEG-rich phase compared to the dextran-rich droplet phase (Fig. 3b), resulting in an increase  
490 in permittivity contrast ( $\epsilon_c - \epsilon_d$ ) with increasing overall polymer concentration. The trends in  
491 Fig. 4d show that permittivity contrast can be precisely tuned by modulating external variables  
492 such as ionic strength or polymer concentration.

493 We then examined whether this permittivity contrast correlates with condensate–membrane  
494 wetting. Figure 4e reveals a linear dependence of the intrinsic contact angle on ( $\epsilon_c - \epsilon_d$ ) across  
495 independent  $\theta_{\square}^{in}$  datasets for various membrane types and condensate systems taken from refs.  
496 <sup>45, 53</sup>. This universal linear correlation suggests a fundamental biophysical mechanism where  
497 the membrane preference between condensed and depleted phases depends primarily on their  
498 permittivity contrast.

499 In first approximation, this trend could be understood considering the membrane adhesion  
500 free energies to the two aqueous phases:  $W_{mc}$  for the condensate and  $W_{me}$  for the depleted phase  
501 (see Methods). Assuming each adhesion energy depends on the permittivity contrast between  
502 the membrane and the respective aqueous phase, ( $\epsilon_c - \epsilon_m$ ) and ( $\epsilon_d - \epsilon_m$ ), the affinity contrast  
503  $W = W_{mc} - W_{me}$  becomes proportional to  $\epsilon_c - \epsilon_d$ . Thus, the intrinsic contact angle, which

504 encodes this affinity contrast, naturally reflects the dielectric difference between the two phases.  
505 Notably, while the intrinsic contact angle defining the membrane-condensate equilibrium  
506 topology explicitly accounts for the influence of condensate surface tension (see Methods), it  
507 is independent from condensate viscosity, which only influences the timescale over which the  
508 membrane-condensate system relaxes to its equilibrium configuration. As we see in Fig. 4e, the  
509 slope and offset of this linear relation are influenced by the membrane lipid composition,  
510 surface charge, and the specific condensate system.

511 Overall, these results underscore the crucial role of permittivity contrasts in modulating  
512 surface affinities between membranous compartments and protein-rich droplets. They highlight  
513 that condensate-membrane interactions cannot be understood by considering the dielectric  
514 properties of the condensates alone; rather, it is the permittivity difference between the  
515 condensed and depleted phases that governs affinity. Significantly, the ability of hydrotropes  
516 like ATP to differentially modulate the permittivity of coexisting phases (Fig. 3h,i) offers a  
517 mechanism to precisely tune condensate recruitment or repulsion from cellular membranes.

518 These findings call for systematic assessment of both phases when probing condensate  
519 interactions with biological materials. Hyperspectral permittivity mapping thus emerges as a  
520 powerful approach for understanding the physical principles that guide biomolecular  
521 condensation and its functional coupling to membrane systems.

522  
523

## DISCUSSION

524 The dielectric permittivity of biomolecular condensates is increasingly recognized as a key  
525 parameter linking their biophysical properties to physiological function<sup>2, 7, 11</sup>. Notably,  
526 permittivity differences between immiscible biopolymer phases govern their interfacial surface  
527 tension<sup>2, 11, 26</sup>, which in turn stabilizes complex core-shell architectures in nuclear organelles<sup>2</sup>.  
528 This interdependence fundamentally arises from a water activity gradient that imposes an  
529 entropic penalty on interfacial water molecules<sup>44, 58, 59</sup>. Consequently, LLPS enables cells to  
530 locally regulate intracellular water activity and internal permittivity, acting as a feedback  
531 mechanism to buffer against osmotic or thermal stress<sup>7, 60</sup>.

532 Our study introduces a powerful hyperspectral imaging approach using the environment-  
533 sensitive fluorophore ACDAN to quantitatively map local dielectric permittivity within  
534 biomolecular condensates and their surrounding environment. This parameter, while crucial for  
535 understanding phase behavior, has remained experimentally elusive, especially in complex,  
536 heterogeneous systems where high resolution and dynamic range are essential. Our method  
537 provides robust, broadband measurements ( $2-80\epsilon_0$ ) independent of solvent chemistry or  
538 instrumental platform. Notably, we reveal a surprisingly wide range of dielectric permittivities  
539 across different condensates, spanning from oil-like ( $\sim 5\epsilon_0$ ) to water-like ( $\sim 60\epsilon_0$ ), see Fig. 2e,  
540 highlighting substantial variability in their hydrophobicity. Importantly, we find that  
541 condensate permittivity is not solely dictated by the type of underlying LLPS interactions (Figs.  
542 2, 3), but is also strongly influenced by the protein-to-water ratio, i.e. water content, within the  
543 condensed phase (Figs. 3b, S5). To confirm this, we performed Raman spectroscopy  
544 measurements (Fig. S9), which revealed that higher-permittivity condensates like K<sub>10</sub>-D<sub>10</sub>  
545 contain more water relative to peptide compared to condensates characterized by lower  
546 permittivity like R<sub>10</sub>-D<sub>10</sub> (Fig. 2); we explore this further in a follow up study<sup>61</sup>.

547 As a note of caution, while water content is a primary determinant of condensate permittivity,  
548 additional effects can dominate in systems containing folded proteins with hydrophobic  
549 microcavities, as exemplified by BSA. In homogeneous BSA solutions, we measure apparent  
550 permittivity values as low as  $\epsilon \approx 25\epsilon_0$  at concentrations of  $\sim 0.05$  mM. While reduced water  
551 dipolar relaxation in protein hydration layers can partially account for this effect<sup>62</sup>, it cannot  
552 explain the nearly order-of-magnitude decrease observed at such low protein volume fractions.

553 We therefore propose that ACDAN partially binds to hydrophobic pockets within folded  
554 BSA, consistent with BSA's known affinity for small ligands. In such environments, water is  
555 highly structured and exhibits an effective permittivity of  $\epsilon \approx 5-6\epsilon_0$ <sup>41</sup>. Dye molecules bound to  
556 these pockets are expected to display enhanced quantum yield<sup>41</sup> (consistent with the markedly  
557 higher ACDAN fluorescence intensity in Fig. 2a), causing protein-associated ACDAN to  
558 dominate the fluorescence signal and, respectively, the permittivity readout.

559 In this regime, ACDAN reports the dielectric properties of its local protein-proximal  
560 microenvironment rather than the bulk-averaged permittivity reflecting the water content.  
561 Nevertheless, the dielectric differences observed in Figs. 3f-j and S8 are biologically relevant,  
562 as enzymatic activity requires a highly hydrated environment capable of sustaining a hydrogen-  
563 bonded water network at the protein surface<sup>63, 64</sup>. In this context, the reduced permittivity  
564 measured in the condensed phase of PEG-BSA systems aligns with reports of decreased  
565 enzymatic activity in the condensed phase of PEG-BSA mixtures compared to homogeneous  
566 BSA solutions of similar overall concentrations<sup>65</sup>.

567 We emphasize that local, protein-proximal sensing of dielectric permittivity by ACDAN is  
568 specific to folded proteins with well-defined hydrophobic cavities, and is not observed for  
569 unstructured polypeptides (K<sub>10</sub>, R<sub>10</sub>, D<sub>10</sub>) or hydrophilic polymers (PDDA, PEG, dextran),  
570 where condensate permittivity is governed primarily by the water-to-polymer ratio (Figs. 3b,  
571 S5) and is independent of dye concentration (for details see ref. <sup>61</sup>).

572 Importantly, this observation highlights that dielectric permittivity in condensates and  
573 solutions of highly structured proteins can be very heterogeneous at the molecular scale and  
574 that local protein-proximal environments may differ substantially from expectations based on  
575 average composition alone. ACDAN-based measurements therefore provide access to the  
576 dielectric microenvironments experienced by proteins and small molecules (i.e. environments  
577 that are likely most relevant for biochemical function), even when these differ from  
578 macroscopic expectations and bulk hydration.

579 Beyond hydration and phase behavior, our high-resolution approach, which allows  
580 simultaneous measurement of both condensed and depleted phases, provides important new  
581 insights into the interactions of condensates with membranes. We find that it is not the absolute  
582 permittivity of condensates, but rather the permittivity contrast with their environment, that is  
583 the central parameter controlling interactions with lipid membranes. A key result of our study  
584 is the discovery of a universal linear relationship between the intrinsic contact angle, which  
585 characterizes membrane-condensate affinity, and the permittivity contrast between the  
586 coexisting phases (Fig. 4e). While many studies focus solely on the properties of the condensate  
587 phase, our findings underscore the critical importance of also characterizing the protein-poor  
588 condensate environment.

589 It is important to distinguish changes in condensate-membrane affinity from variations in  
590 the free energy of demixing. If these quantities were directly coupled, one would expect the

591 intrinsic contact angle in the glycinin-membrane system to exhibit a maximum at the point of  
592 largest separation from both the upper and lower binodals in Fig. 3c, where the thermodynamic  
593 driving force for phase separation is maximal. Instead, the intrinsic contact angle increases  
594 monotonically with NaCl concentration<sup>53</sup>. This behavior is consistent with the observed  
595 evolution of the permittivity contrast: while the permittivity of the dense phase remains largely  
596 insensitive to salt, that of the dilute phase decreases continuously (Fig. 4c). These trends  
597 indicate that membrane affinity is governed by phase-specific dielectric properties rather than  
598 by the demixing free energy alone. Additional contributions may arise from NaCl-dependent  
599 changes in protein conformation, as suggested previously<sup>14</sup>.

600 Beyond thermodynamic considerations, membrane-condensate interactions emerge from a  
601 multifaceted interplay of molecular polarity, surface orientation, charge, and ion partitioning.  
602 While previous studies have explored the effect of condensate surface potential, ionic strength<sup>53</sup>  
603 and protein sequence<sup>37</sup>, our results extend this framework by identifying dielectric permittivity  
604 as a quantitative, bulk parameter that directly governs condensate-membrane interactions,  
605 revealing an additional and previously unrecognized physical determinant of wetting behavior.

606 Given that the hydrophobic core of lipid membranes exhibits a low permittivity (comparable  
607 to oils), condensates with inherently low dielectric permittivity are likely to exhibit greater  
608 affinity to membranes. At comparable permittivity contrasts, we speculate that such  
609 condensates, like glycinin and BSA-PEG (Fig. 2e), will display enhanced membrane wetting  
610 compared to more hydrophilic, high-permittivity condensates, such as K<sub>10</sub>-D<sub>10</sub>, ATP-PDDA  
611 and the dextran-rich phase in PEG-dextran ATPS (Figs. 2e and 3b). The membrane surface  
612 charge further modulates this interaction: achieving the same intrinsic contact angle on charged  
613 membranes requires a higher permittivity contrast than on neutral membranes (Fig. 4e).  
614 Together, these observations indicate that membrane-condensate interactions arise from  
615 competing contributions: for highly charged membranes, surface electrostatics dominate and  
616 largely mask dielectric effects, whereas for weakly charged membranes, the bulk permittivity  
617 contrast between dense and dilute phases becomes the primary determinant of condensate  
618 affinity. Similarly, more ordered (and presumably more hydrophobic due to higher lipid  
619 packing) membranes demand larger permittivity contrasts to reach comparable wetting, likely  
620 due to their lower intrinsic permittivity.

621 We also propose that lower-permittivity condensates may preferentially stabilize  
622 hydrophobic membrane defects like pores, a property with potential relevance for cellular  
623 membrane repair. In this context, condensates can act as plugs for transient membrane pores,  
624 helping to stabilize and reseal damaged membrane organelles<sup>5, 66</sup>. Condensates with lower  
625 permittivity may likely allow better integration with the hydrophobic membrane environment,  
626 facilitating pore sealing and restoring membrane integrity.

627 Beyond these fundamental insights, our method provides a sensitive dielectric descriptor of  
628 coexisting phases across different regions of a phase diagram (Fig. 3). While it does not yield  
629 a direct readout of phase composition, it robustly captures relative changes in the  
630 physicochemical environments of dense and dilute phases, allowing the quantification of subtle  
631 changes induced by hydrotropes like ATP (Fig. 3h,i). Considering ATP's central role in cellular  
632 physiology, our results suggest that ATP not only influences protein solubility<sup>35, 50</sup> but also acts  
633 as a key modulator of condensate interactions with other cellular components, by affecting  
634 permittivity contrast between coexisting phases.

635 Overall, our results underscore the utility of this method in mapping fine variations in phase  
636 behavior, composition, and dielectric properties with high spatial resolution and across diverse  
637 biomolecular condensate systems. We believe these findings significantly advance the physical  
638 framework for understanding the interplay between electrostatics, phase separation, and  
639 biological function in complex and heterogeneous biomolecular systems and in understanding  
640 condensate interactions. Given the accessibility of hyperspectral imaging on commercial  
641 confocal microscopes<sup>67</sup>, the method is poised to become a valuable tool for studying dynamic  
642 intracellular environments and advancing the understanding of biomolecular phase transitions  
643 in health and disease. The approach paves the way for new investigations into the  
644 physicochemical mechanisms underlying condensate function, aging and liquid-to-solid  
645 transitions associated with neurodegenerative pathologies<sup>28, 68</sup>.

## 646 **METHODS**

### 647 **Materials**

648 6-acetyl-2-dimethylaminonaphthalene (ACDAN) was purchased from Santa Cruz  
649 Biotechnology (USA). Polydiallyldimethylammonium chloride (PDDA, 200-350 kDa, 20 wt%  
650 solution in water), adenosine triphosphate (ATP) and sodium hydroxide (NaOH) were obtained  
651 from Sigma-Aldrich (Missouri, USA). Poly(ethylene glycol) (PEG 8000, Mw 8kg/mol and  
652 PEG 400, Mw 4kg/mol) and dextran from *Leuconostoc mesenteroides* (molecular weight  
653 between 400 kDa and 500 kDa) were purchased from Sigma-Aldrich. The oligopeptides, poly-  
654 L-lysine hydrochloride (degree of polymerization,  $n = 10$ ;  $K_{10}$ ), poly and poly-L-aspartic acid  
655 sodium salt ( $n=10$ ;  $D_{10}$ ) were purchased from Alamanda Polymers (AL, USA) and used without  
656 further purification ( $\geq 95\%$ ). BSA ( $\geq 98\%$  purity, 66kg/mol), MBP bovine ( $\geq 90\%$ ), 1,4-Dioxane,  
657 Anisol (99%), 1-Hexanol and 1-Butanol (99.9%) were purchased from Sigma-Aldrich. Mineral  
658 oil was purchased from Carl Roth GmbH. Ethanol absolute was purchased from VWR  
659 chemicals BDH. Phosphate buffered saline (PBS) pH 7.2 was purchased from Thermofisher.  
660 Polyvinyl alcohol (PVA, Mw 145000kg/mol) was purchased from Merck (Darmstadt,  
661 Germany). All solutions were prepared using ultrapure water from SG water purification system  
662 (Ultrapure Integra UV plus, SG Wasseraufbereitung) with a resistivity of 18.2 M $\Omega$  cm.  
663

### 664 **Condensate formation and labelling**

665 Coverslips for confocal microscopy (26×56 mm, Waldemar Knittel Glasbearbeitungs  
666 GmbH, Germany) were washed with ethanol and water, then passivated with a 10 mg/mL BSA  
667 solution and an aliquot of 10 $\mu$ L of condensates suspension was placed on the coverslip before  
668 imaging.

669 *PDDA-ATP condensates*: Phase separated droplets were formed by gently mixing aliquots  
670 of stock solutions of ATP and PDDA (in this order) with ACDAN in pure water to a final  
671 volume of 10  $\mu$ L. The final concentration of each component was as follows: 14.8 mM ATP,  
672 4.9 mM PDDA, 10 $\mu$ M ACDAN.

673 *Glycinin condensates*: Freeze-dried glycinin was a gift from Dr. Nannan Chen. The  
674 purification is detailed in ref<sup>48</sup>. A 20 mg/mL glycinin solution at pH 7 was freshly prepared in  
675 ultrapure water and filtered with 0.45  $\mu$ m filters to remove any insoluble materials. To form the  
676 condensates, the desired volume of the glycinin solution was mixed with the same volume of a  
677 NaCl solution of twice the desired final concentration. In this manner, the final protein  
678 concentration was 10 mg/mL<sup>48</sup>. The final concentration of ACDAN was 5 $\mu$ M.

679 *K<sub>10</sub>-D<sub>10</sub> and R<sub>10</sub>-D<sub>10</sub> condensates:* Phase separated droplets were formed by gently mixing  
680 aliquots of stock solutions of D<sub>10</sub> and K<sub>10</sub> or R<sub>10</sub> (in this order) with ACDAN in pure water to a  
681 final volume of 10  $\mu$ L. The final concentration of each component was as follows: 2.5 mM D<sub>10</sub>,  
682 2.5 mM K<sub>10</sub> or R<sub>10</sub>, 15 $\mu$ M ACDAN.

683 *PEG-BSA condensates:* Phase separated droplets were formed by gently mixing aliquots (via  
684 pipetting and releasing 3 times the total volume) in a 1:1 ratio of stock solutions of 20% PEG-  
685 8000 in PBS with 30 $\mu$ M ACDAN with BSA dissolved in PBS at half the desired concentration  
686 and to a final volume of 10  $\mu$ L.

687 *PEG-Dextran condensates:* A polymer solution in composed of the desired weight fractions  
688 of PEG and dextran were prepared and left, when relevant, for 2 days to completely phase  
689 separate and equilibrate. ACDAN was then added to each phase to reach a final concentration  
690 of 25 $\mu$ M of ACDAN.

691 *MBP condensates:* MBP condensates were prepared by following the procedure described  
692 in <sup>69</sup>. Briefly, a 5mg/mL solution of MBP dissolved in water was mixed with a 20mM NaOH  
693 solution of 10 $\mu$ M ACDAN in a 1:1 ratio.

#### 694 **Confocal microscopy and hyperspectral imaging**

695 Hyperspectral images were acquired using a confocal Leica SP8 FALCON microscope  
696 equipped with a 63 $\times$ , 1.2 NA water immersion objective (Leica, Mannheim, Germany). The  
697 microscope was coupled to a pulsed Ti:Sapphire laser MaiTai (SpectraPhysics, USA), with a  
698 repetition rate of 80 MHz. A two-photon wavelength of 780 nm was used for ACDAN  
699 excitation. Image acquisition was performed with a frame size of 512  $\times$  512 pixels<sup>14, 53</sup> and a  
700 pixel size of 72 nm $\times$ 72 nm using a Hyd SMD detector in standard mode. For hyperspectral  
701 imaging, the xy $\lambda$  configuration of Leica SP8 was used, sequentially measuring in 32 channels  
702 with a bandwidth of 9.75 nm in the range from 416 to 728 nm. Some hyperspectral images were  
703 realigned using the ImageJ software and all hyperspectral stacks were processed by the SimFCS  
704 software developed at the Laboratory of Fluorescence Dynamics (available at  
705 <https://www.lfd.uci.edu/globals/>), and analyzed using Python code based in the PhasorPy  
706 library (available at <https://www.phasorpy.org/>).

#### 707 **Gaussian fit analysis**

708 The Gaussian fit analysis of ACDAN hyperspectral imaging data consists in approximating  
709 the wavelength-intensity profile of ACDAN emission by a skewed Gaussian function of the  
710 form:

$$711 \quad I(\lambda) = I_0 \Psi \left( \frac{\lambda - \mu}{\sigma} \right) \Phi \left( \gamma \left( \frac{\lambda - \mu}{\sigma} \right) \right), \quad (M1)$$

$$712 \quad \Psi(x) = \frac{1}{\sqrt{2\pi}} \exp \left( -\frac{x^2}{2} \right), \quad (M2)$$

$$713 \quad \Phi(x) = \frac{1}{2} \left( 1 + \operatorname{erf} \left( \frac{x}{\sqrt{2}} \right) \right), \quad (M3)$$

714 where  $\Psi$ ,  $\Phi$ ,  $\operatorname{erf}$ ,  $\lambda$ ,  $\mu$ ,  $\sigma$ ,  $I_0$  and  $\gamma$  respectively represent the normal distribution function, the  
715 cumulative distribution function, the error function, the wavelength, the mean wavelength, the  
716 mean deviation, the intensity scaling factor and the skewness factor. Data interpolation was  
717 performed based on computer programming script written in Python and based on the scipy  
718 library. The  $\lambda_{max}$  was then evaluated based on the position of the maximum of the fitted

719 ACDAN emission curve and used as an input in the  $\lambda - \varepsilon$  calibration curves presented in Figs.  
 720 1e and S1 in the main text.

### 721 **Spectral phasor analysis**

722 The spectral phasor analysis of ACDAN hyperspectral imaging data consists in calculating  
 723 the real and imaginary components of the Fourier transform, respectively referred to as  $G$  and  
 724  $S$ , and using them as Cartesian coordinates on a 2D spectral phasor map. ( $G, S$ ) are defined by  
 725 the following expressions:

$$726 \quad G = \frac{\int_{\lambda_0}^{\lambda_f} I(\lambda) \cos(\omega n(\lambda - \lambda_0)) d\lambda}{\int_{\lambda_0}^{\lambda_f} I(\lambda) d\lambda}, \quad (\text{M4})$$

$$727 \quad S = \frac{\int_{\lambda_0}^{\lambda_f} I(\lambda) \sin(\omega n(\lambda - \lambda_0)) d\lambda}{\int_{\lambda_0}^{\lambda_f} I(\lambda) d\lambda}, \quad (\text{M5})$$

728 where  $I(\lambda)$  for a particular pixel represents the intensity as a function of wavelength, measured  
 729 in the interval  $(\lambda_0; \lambda_f)$ . This range depends on instrumental constraints and the type of detector  
 730 used for the analysis, in our case 416–728 nm. Note that changing the detection range will  
 731 necessarily results in a change of the relative positions of different points on the phasor plot;  
 732 therefore, the detection range must be conserved across all experiments in order to be able to  
 733 compare measurements. The parameter  $n$  is the harmonic, i.e. the number of cycles of the  
 734 trigonometric function that are fit in the wavelength range by means of the angular frequency  
 735  $\omega$ :

$$736 \quad \omega = \frac{2\pi}{(\lambda - \lambda_0)} \quad (\text{M6})$$

737 When imaging with a microscope, we acquire a discrete number of spectral steps  
 738 corresponding to the number of detection windows that cover the spectral range. For  
 739 computational purposes, the spectral phasor transform is expressed as a discretized  
 740 approximation of the continuous transform as:

$$741 \quad G = \frac{\sum_c^{N_c} I(c) \cos(2\pi c/N_c)}{\sum_c^{N_c} I(c)}, \quad (\text{M7})$$

$$742 \quad S = \frac{\sum_c^{N_c} I(c) \sin(2\pi c/N_c)}{\sum_c^{N_c} I(c)}, \quad (\text{M8})$$

743 where  $I(c)$  is the pixel intensity at channel and  $c$  is the total number of channels. Conveniently,  
 744 even if the total number of spectral acquisition channels is small (in our case 32), the coordinates  
 745  $S$  and  $G$  can be considered quasi-continuous, since the photon counts in each pixel and channel  
 746 are high enough ( $\sim 102$ ) to allow a wide range of possible values of the coordinates  $S$  and  $G$ .

747 The spectral phasor approach obeys the rules of vector algebra, known as the linear  
 748 combination of phasors. This property implies that a combination of two independent  
 749 fluorescent species will appear on the phasor plot at a position that is a linear combination of  
 750 the phasor positions of the two independent spectral species. The fraction of each component  
 751 can be determined from the coefficients of the linear combination.

752 Note that the phase angle  $\phi$ , and the modulus,  $M$  can be obtained through:

$$753 \quad \phi = \arctan\left(\frac{S}{G}\right) \quad (\text{M9})$$

$$754 \quad M = \sqrt{S^2 + G^2} \quad (\text{M10})$$

755 Data processing and spectral phasor analysis were performed by first converting the Image  
 756 stacks into .r64 files using the SimFCS software developed at the Laboratory of Fluorescence  
 757 Dynamics, available on the webpage (<https://www.lfd.uci.edu/globals/>), and further processed  
 758 using Python programming code based on the PhasorPy library (<https://www.phasorpy.org/>).  
 759

### 760 **Relating contact angles, mechanical parameters and permittivity contrast**

761 This section is based on the theoretical framework derived in ref. <sup>53</sup>. Briefly, the contact  
 762 angles in Fig. 4a, are related to the force balance between the different surface tensions of the  
 763 three surface segments pulling along the membrane-condensate contact line. One of these  
 764 tensions is the interfacial tension of the condensate-buffer interface  $\Sigma_{ce}$  (see Fig. 4a). The other  
 765 two are the mechanical tensions of the two membrane segments in contact with the depleted  
 766 phase ( $\Sigma_{ie}^m$ ) and condensate ( $\Sigma_{ic}^m$ ), given by<sup>55</sup>:

$$767 \quad \Sigma_{ic}^m = \Sigma + W_{mc} \quad \text{and} \quad \Sigma_{ie}^m = \Sigma + W_{me} \quad (\text{M11})$$

768 where  $\Sigma$  denotes the lateral stress within the membrane, whereas  $W_{mc}$  and  $W_{me}$  represent the  
 769 adhesion free energies per unit area of the condensate and of the external depleted phase,  
 770 relative to the interior solution<sup>55</sup>. The affinity contrast between the condensate and the external  
 771 buffer is then given by<sup>55</sup> :

$$772 \quad W = \Sigma_{ic}^m - \Sigma_{ie}^m = W_{mc} - W_{me} \quad (\text{M12})$$

773 The geometry-dependent lateral membrane stress  $\Sigma$  drops out from the affinity contrast  $W$   
 774 which is negative if the membrane prefers the condensate phase over the external buffer, and  
 775 positive otherwise. The force balance in Fig. 4a also implies the geometric relationships<sup>55</sup>

$$776 \quad \frac{\Sigma_{ie}^m}{\Sigma_{ce}} = \frac{\sin \theta_c}{\sin \theta_i} \quad \text{and} \quad \frac{\Sigma_{ic}^m}{\Sigma_{ce}} = \frac{\sin \theta_e}{\sin \theta_i} \quad (\text{M13})$$

777 between the surface tensions and the contact angles, as follows from the law of sines for the  
 778 tension triangle in Fig. 4a. When we introduce Eqs. (M11) and take the difference of the two  
 779 equations in Eq. (M13), for the affinity contrast  $W$  in Eq. (M12) we arrive at

$$780 \quad W = \cos \theta_{ce}^{in} \Sigma_{ce} \quad \text{where} \quad \cos \theta_{ce}^{in} \equiv \frac{\sin \theta_e - \sin \theta_c}{\sin \theta_i} \quad (\text{M14})$$

781 Thus, the rescaled affinity contrast,  $W/\Sigma_{ce}$ , which is a mechanical quantity related to the  
 782 adhesion free energies of the membrane segments, is equal to  $\cos \theta_{ce}^{in}$ , where the intrinsic  
 783 contact angle  $\theta_{ce}^{in}$  is a scale-invariant material parameter.  
 784  
 785

### 786 **ACKNOWLEDGEMENTS**

787 A.M. acknowledges support from Alexander von Humboldt Foundation and CONICET. We  
 788 acknowledge Nannan Chen for providing glycinin, and Clemens Schmitt for the assistance with  
 789 Raman experiments. We also acknowledge support from the German Academic Exchange  
 790 Service (Deutscher Akademischer Austauschdienst, DAAD) in the framework of projects  
 791 57654674 and 57701619. R.D. acknowledges the ComeInCell network funded by the European  
 792 Union's Horizon Europe research and innovation program under the Marie Skłodowska-Curie  
 793 grant agreement No. 101168939. We would like to thank Dr. Leonel Malacrida for the helpful  
 794 discussions regarding ACDAN hyperspectral imaging and fluorescence mechanisms.  
 795  
 796

797  
798  
799  
800  
801  
802  
803  
804  
805  
806  
807  
808  
809  
810  
811  
812  
813  
814  
815  
816  
817  
818  
819  
820  
821  
822  
823  
824  
825  
826  
827  
828  
829  
830  
831  
832  
833  
834  
835  
836  
837  
838  
839  
840  
841  
842  
843  
844  
845  
846  
847

## REFERENCES

1. Decker, C.J. & Parker, R. P-bodies and stress granules: possible roles in the control of translation and mRNA degradation. *Cold Spring Harbor perspectives in biology* **4**, a012286 (2012).
2. Feric, M. et al. Coexisting Liquid Phases Underlie Nucleolar Subcompartments. *Cell* **165**, 1686-1697 (2016).
3. Feric, M. et al. Mesoscale structure–function relationships in mitochondrial transcriptional condensates. *Proceedings of the National Academy of Sciences* **119**, e2207303119 (2022).
4. Fei, J. et al. Quantitative analysis of multilayer organization of proteins and RNA in nuclear speckles at super resolution. *Journal of cell science* **130**, 4180-4192 (2017).
5. Bussi, C. et al. Stress granules plug and stabilize damaged endolysosomal membranes. *Nature* **623**, 1062-1069 (2023).
6. Alberti, S. & Hyman, A.A. Biomolecular condensates at the nexus of cellular stress, protein aggregation disease and ageing. *Nature Reviews Molecular Cell Biology* **22**, 196-213 (2021).
7. Watson, J.L. et al. Macromolecular condensation buffers intracellular water potential. *Nature* **623**, 842-852 (2023).
8. Lyon, A.S., Peeples, W.B. & Rosen, M.K. A framework for understanding the functions of biomolecular condensates across scales. *Nat Rev Mol Cell Biol* **22**, 215-235 (2021).
9. Smokers, I.B., Visser, B.S., Slootbeek, A.D., Huck, W.T. & Spruijt, E. How Droplets Can Accelerate Reactions– Coacervate Protocells as Catalytic Microcompartments. *Accounts of Chemical Research* **57**, 1885-1895 (2024).
10. Jawerth, L. et al. Protein condensates as aging Maxwell fluids. *Science* **370**, 1317-1323 (2020).
11. Ye, S. et al. Micropolarity governs the structural organization of biomolecular condensates. *Nature Chemical Biology* **20**, 443-451 (2024).
12. Alshareedah, I. et al. Sequence-specific interactions determine viscoelasticity and ageing dynamics of protein condensates. *Nature Physics* **20**, 1482-1491 (2024).
13. Joshi, A. et al. Hydrogen-Bonded Network of Water in Phase-Separated Biomolecular Condensates. *The Journal of Physical Chemistry Letters* **15**, 7724-7734 (2024).
14. Mangiarotti, A. et al. Biomolecular condensates modulate membrane lipid packing and hydration. *Nature Commun.* **14**, 6081 (2023).
15. Dogra, P., Joshi, A., Majumdar, A. & Mukhopadhyay, S. Intermolecular charge-transfer modulates liquid–liquid phase separation and liquid-to-solid maturation of an intrinsically disordered pH-responsive domain. *Journal of the American Chemical Society* **141**, 20380-20389 (2019).
16. Dai, Y. et al. Interface of biomolecular condensates modulates redox reactions. *Chem* **9**, 1594-1609 (2023).
17. Zhu, L., Pan, Y., Hua, Z., Liu, Y. & Zhang, X. Ionic effect on the microenvironment of biomolecular condensates. *Journal of the American Chemical Society* **146**, 14307-14317 (2024).
18. Cui, J. et al. Mitochondria-targeted ratiometric fluorescent probes for micropolarity and microviscosity and their applications. *Chinese Chemical Letters* **30**, 1071-1074 (2019).
19. Xiao, H., Li, P. & Tang, B. Recent progresses in fluorescent probes for detection of polarity. *Coordination Chemistry Reviews* **427**, 213582 (2021).
20. Levitt, J.A., Chung, P.-H. & Suhling, K. Spectrally resolved fluorescence lifetime imaging of Nile red for measurements of intracellular polarity. *Journal of biomedical optics* **20**, 096002-096002 (2015).
21. Yang, Z. et al. A Nile Red/BODIPY-based bimodal probe sensitive to changes in the micropolarity and microviscosity of the endoplasmic reticulum. *Chemical Communications* **50**, 11672-11675 (2014).
22. Vorontsova, I. et al. In vivo macromolecular crowding is differentially modulated by aquaporin 0 in zebrafish lens: Insights from a nanoenvironment sensor and spectral imaging. *Science Advances* **8**, eabj4833 (2022).

- 848 23. Schlüßler, R. et al. Correlative all-optical quantification of mass density and mechanics of  
849 subcellular compartments with fluorescence specificity. *Elife* **11**, e68490 (2022).
- 850 24. Hong, Y. et al. Label-free quantitative analysis of Coacervates via 3D phase imaging. *Advanced*  
851 *Optical Materials* **9**, 2100697 (2021).
- 852 25. Linsenmeier, M. et al. Dynamic arrest and aging of biomolecular condensates are modulated  
853 by low-complexity domains, RNA and biochemical activity. *Nature Communications* **13**, 3030  
854 (2022).
- 855 26. Zhu, L., Pan, Y., Hua, Z., Liu, Y. & Zhang, X. Ionic Effect on the Microenvironment of  
856 Biomolecular Condensates. *Journal of the American Chemical Society* (2024).
- 857 27. Wu, T. et al. Single-fluorogen imaging reveals distinct environmental and structural features of  
858 biomolecular condensates. *Nature Physics* **21**, 778-786 (2025).
- 859 28. Rodríguez, L.C., Foressi, N.N. & Celej, M.S. Tracking protein transitions through fluorescence  
860 spectral phasor analysis with ACDAN. *Biophysical Reports* **5** (2025).
- 861 29. Wang, L. et al. Xanthone-based solvatochromic fluorophores for quantifying micropolarity of  
862 protein aggregates. *Chemical Science* **13**, 12540-12549 (2022).
- 863 30. Weber, G. & Farris, F.J. Synthesis and spectral properties of a hydrophobic fluorescent probe:  
864 6-propionyl-2-(dimethylamino) naphthalene. *Biochemistry* **18**, 3075-3078 (1979).
- 865 31. Gunther, G., Malacrida, L., Jameson, D.M., Gratton, E. & Sánchez, S.A. LAURDAN since Weber:  
866 the quest for visualizing membrane heterogeneity. *Accounts of chemical research* **54**, 976-987  
867 (2021).
- 868 32. Thoke, H.S. et al. Tight coupling of metabolic oscillations and intracellular water dynamics in  
869 *Saccharomyces cerevisiae*. *PLoS One* **10**, e0117308 (2015).
- 870 33. Thoke, H.S., Thorsteinsson, S., Stock, R.P., Bagatolli, L.A. & Olsen, L.F. The dynamics of  
871 intracellular water constrains glycolytic oscillations in *Saccharomyces cerevisiae*. *Scientific*  
872 *Reports* **7**, 16250 (2017).
- 873 34. Begarani, F. et al. Capturing metabolism-dependent solvent dynamics in the lumen of a  
874 trafficking lysosome. *ACS nano* **13**, 1670-1682 (2019).
- 875 35. Bagatolli, L.A. To see or not to see: Lateral organization of biological membranes and  
876 fluorescence microscopy. *Biochim. Biophys. Acta-Biomembr.* **1758**, 1541-1556 (2006).
- 877 36. Mangiarotti, A. et al. Lipid packing and cholesterol content regulate membrane wetting and  
878 remodeling by biomolecular condensates. *Nature Commun.* **16**, 2756 (2025).
- 879 37. Holland, J., Nott, T.J. & Aarts, D.G.A.L. Intrinsic hydrophobicity of IDP-based biomolecular  
880 condensates drives their partial drying on membrane surfaces. *The Journal of Chemical Physics*  
881 **162** (2025).
- 882 38. Lakowicz, J. Principles of fluorescence spectroscopy. *University of Maryland School of Medicine*  
883 *Baltimore* **132** (2006).
- 884 39. Myroshnychenko, V. & Brosseau, C. Finite-element modeling method for the prediction of the  
885 complex effective permittivity of two-phase random statistically isotropic heterostructures.  
886 *Journal of applied physics* **97** (2005).
- 887 40. Jiménez-Sánchez, A., Lei, E.K. & Kelley, S.O. A multifunctional chemical probe for the  
888 measurement of local micropolarity and microviscosity in mitochondria. *Angewandte Chemie*  
889 *International Edition* **57**, 8891-8895 (2018).
- 890 41. Fernandes, A.J.F.C. et al. 4-Dimethylamino-beta-nitrostyrene, a fluorescent solvatochromic  
891 probe to estimate the apparent dielectric constant in serum albumin: Experimental and  
892 molecular dynamics studies. *J. Photochem. Photobiol. A: Chem.* **433**, 114197 (2022).
- 893 42. Fossat, M.J., Zeng, X. & Pappu, R.V. Uncovering differences in hydration free energies and  
894 structures for model compound mimics of charged side chains of amino acids. *The Journal of*  
895 *Physical Chemistry B* **125**, 4148-4161 (2021).
- 896 43. Armentia, L., López, X. & De Sancho, D. Arginine versus Lysine: Molecular Determinants of  
897 Cation- $\pi$  Interactions in Biomolecular Condensates. *bioRxiv*, 2025.2010. 2001.679751 (2025).

- 898 44. Socas, L.B.P. & Ambroggio, E.E. Linking surface tension to water polarization with a new  
899 hypothesis: The Ling-Damodaran Isotherm. *Colloids and Surfaces B: Biointerfaces* **230**, 113515  
900 (2023).
- 901 45. Liu, Y., Agudo-Canalejo, J., Grafmüller, A., Dimova, R. & Lipowsky, R. Patterns of Flexible  
902 Nanotubes Formed by Liquid-Ordered and Liquid-Disordered Membranes. *ACS Nano* **10**, 463-  
903 474 (2016).
- 904 46. Liu, Y., Lipowsky, R. & Dimova, R. Concentration Dependence of the Interfacial Tension for  
905 Aqueous Two-Phase Polymer Solutions of Dextran and Polyethylene Glycol. *Langmuir* **28**,  
906 3831-3839 (2012).
- 907 47. Sato, T., Niwa, H., Chiba, A. & Nozaki, R. Dynamical structure of oligo (ethylene glycol) s-water  
908 solutions studied by time domain reflectometry. *The Journal of chemical physics* **108**, 4138-  
909 4147 (1998).
- 910 48. Chen, N., Zhao, Z., Wang, Y. & Dimova, R. Resolving the mechanisms of soy glycinin self-  
911 coacervation and hollow-condensate formation. *ACS macro letters* **9**, 1844-1852 (2020).
- 912 49. Kunz, W., Holmberg, K. & Zemb, T. Hydrotropes. *Current Opinion in Colloid & Interface Science*  
913 **22**, 99-107 (2016).
- 914 50. Patel, A. et al. ATP as a biological hydrotrope. *Science* **356**, 753-756 (2017).
- 915 51. Saurabh, S. et al. ATP-responsive biomolecular condensates tune bacterial kinase signaling. *Sci*  
916 *Adv* **8**, eabm6570 (2022).
- 917 52. Li, Y., Lipowsky, R. & Dimova, R. Transition from complete to partial wetting within membrane  
918 compartments. *Journal of the American Chemical Society* **130**, 12252-12253 (2008).
- 919 53. Mangiarotti, A., Chen, N., Zhao, Z., Lipowsky, R. & Dimova, R. Wetting and complex remodeling  
920 of membranes by biomolecular condensates. *Nature communications* **14**, 2809 (2023).
- 921 54. Mangiarotti, A. & Dimova, R. Biomolecular Condensates in Contact with Membranes. *Annu.*  
922 *Rev. Biophys.* **53**, 319-341 (2024).
- 923 55. Lipowsky, R. Response of membranes and vesicles to capillary forces arising from aqueous two-  
924 phase systems and water-in-water droplets. *The Journal of Physical Chemistry B* **122**, 3572-  
925 3586 (2018).
- 926 56. Zhao, Z. et al. Super-Resolution Imaging of Highly Curved Membrane Structures in Giant  
927 Vesicles Encapsulating Molecular Condensates. *Adv. Mater.* **34**, 2106633 (2022).
- 928 57. Kusumaatmaja, H., Li, Y., Dimova, R. & Lipowsky, R. Intrinsic Contact Angle of Aqueous Phases  
929 at Membranes and Vesicles. *Phys. Rev. Lett.* **103**, 238103 (2009).
- 930 58. Kumar, R., Sumpter, B.G. & Muthukumar, M. Enhanced Phase Segregation Induced by Dipolar  
931 Interactions in Polymer Blends. *Macromolecules* **47**, 6491-6502 (2014).
- 932 59. Ling, G.N. Life at the cell and below-cell level: The hidden history of a fundamental revolution  
933 in biology. (Pacific Press New York, 2001).
- 934 60. Mukherjee, S. & Schäfer, L. (2023).
- 935 61. Sabri, E., Mangiarotti, A., Schmitt, C. & Dimova, R. Label-free in situ approach for characterizing  
936 the macromolecular composition and water content in biomolecular condensates. *bioRxiv*,  
937 2025.2010.2020.683555 (2025).
- 938 62. Ghosh, R., Banerjee, S., Hazra, M., Roy, S. & Bagchi, B. Sensitivity of polarization fluctuations  
939 to the nature of protein-water interactions: Study of biological water in four different protein-  
940 water systems. *The Journal of Chemical Physics* **141** (2014).
- 941 63. Smolin, N., Oleinikova, A., Brovchenko, I., Geiger, A. & Winter, R. Properties of spanning water  
942 networks at protein surfaces. *The Journal of Physical Chemistry B* **109**, 10995-11005 (2005).
- 943 64. Nakasako, M. Water-protein interactions from high-resolution protein crystallography.  
944 *Philosophical Transactions of the Royal Society of London. Series B: Biological Sciences* **359**,  
945 1191-1206 (2004).
- 946 65. Lamy, H. et al. Kinetic Study of the Esterase-like Activity of Albumin following Condensation by  
947 Macromolecular Crowding. *Biomacromolecules* **25**, 2803-2813 (2024).
- 948 66. Janssen, A.F.J. et al. Patching up the nucleus: a novel role for PMLII in nuclear envelope rupture  
949 repair. *bioRxiv*, 2025.2001.2024.634656 (2025).

- 950 67. Zimmermann, T., Rietdorf, J. & Pepperkok, R. Spectral imaging and its applications in live cell  
951 microscopy. *FEBS Lett* **546**, 87-92 (2003).
- 952 68. Patel, A. et al. A liquid-to-solid phase transition of the ALS protein FUS accelerated by disease  
953 mutation. *Cell* **162**, 1066-1077 (2015).
- 954 69. Aggarwal, S. et al. Myelin membrane assembly is driven by a phase transition of myelin basic  
955 proteins into a cohesive protein meshwork. *PLoS biology* **11**, e1001577 (2013).
- 956